Chapter 4

Flexible Asymmetric Supercapacitor Based on Functionalized Reduced Graphene Oxide Aerogels with Wide Working Potential Window

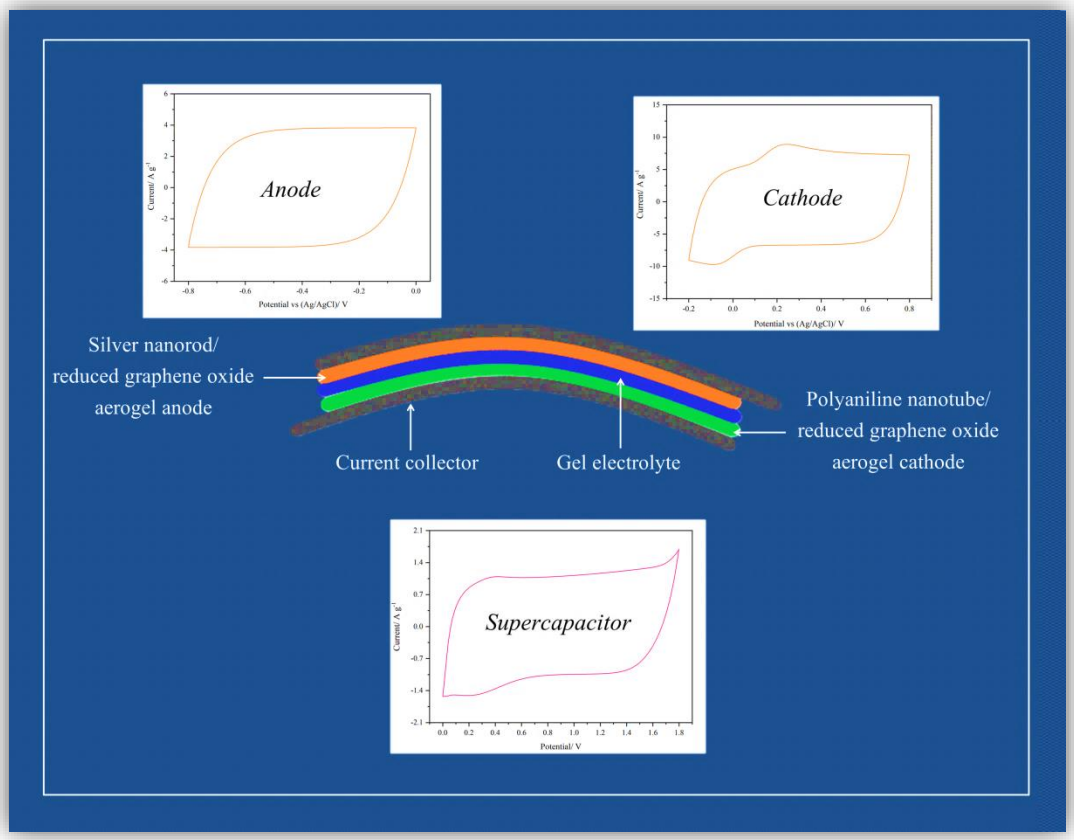

Reduced graphene oxide aerogel is functionalized separately with silver nanorod and polyaniline nanotube to act respectively as the anode and the cathode in a flexible asymmetric supercapacitor with a wide working potential window of 1.8 V.

4.1 Introduction

In the recent years, energy storage devices have attracted intensive attention, owing to the tremendous interest in portable electronics. Supercapacitors, particularly, are equipped with high power density and fast charge discharge capability along with the added advantages of being flexible and lightweight [1,2]. Nonetheless, the commercially available supercapacitors still suffer from low energy densities which make them incompetent to replace batteries as power sources. The energy density (E) of a capacitor is given by the equation: $E = ½ CV^2$, where C and V represent cell capacitance and cell voltage respectively. The voltage plays a major role in determining the energy density of a supercapacitor. A most promising approach to manipulate the working voltage window is by preparing asymmetric supercapacitors (ASCs) with dissimilar electrodes. In such a device, two different electrode materials are used: the negative electrode, generally an electrochemical double-layer capacitor (EDLC) is the power source while the positive electrode, a pseudo-capacitor, is the energy source. This can be considered as a win–win scenario where both non-faradaic and faradaic capacitors work in tandem to deliver a storage system of high power and energy density [3].

Graphene has emerged as an excellent electrode material, primarily because of its high electrical conductivity, good cycling stability, excellent specific surface area and superior mechanical flexibility [4]. The surface area of a single graphene sheet is 2630 $m^2 g^{-1}$ while it can fundamentally provide specific capacitance (C_{sp}) of 550 F g^{-1} [5]. Despite these phenomenal properties, an undesirable yet inevitable problem with graphene is that they undergo restacking due to π-π interactions and the van der Waals forces between them. Formation of electrical double layers becomes difficult as the ions cannot get access to the inner layers of stacked graphene [6].The electrochemistry of a supercapacitor is a two-dimensional science since charging or discharging of the electrodes proceeds on the surfaces rather than in bulk. When the condition of two- dimensionality is imposed, certain diffusion limitations come into effect. These problems can be attenuated with the use of high surface area and porous electrodes, having a quasi-three dimensional nature [7].Three-dimensional graphene aerogel comes across as a

---

This part of the thesis is published in:

Bora, A., Mohan, K., Doley, S., and Dolui, S. K. Flexible asymmetric supercapacitor based on functionalized reduced graphene oxide aerogels with wide working potential window.*ACS Applied Materials & Interfaces*, 10(9):7996-8009, 2018.

favorable candidate for such an application. Since its invention in 1931 by S. S. Kistler[8], aerogels are being increasingly recognized as a very useful material that present fascinating and unique features like ultra-light weight, high specific surface area and high porosity [9]. Due to the high volume of pores, the outermost graphene sheets can be easily wetted by the electrolyte. This causes quick charge and discharge of the supercapacitors [10].

Metal oxides like manganese dioxide (MnO_2) and intrinsically conducting polymers such as polyaniline (PAni) and polypyrrole (PPy) are popular filler materials which are incorporated into the aerogel network to improve their capacitive behavior [11,12]. PAni, in particular, has shown great potential as a pseudo-capacitive electrode material due to high electrical conductivity, mechanical flexibility and cost effectiveness [13]. Furthermore, devices based on PAni have better energy densities as compared to EDLCs [14,15].PAni, in nanotubular form, has an advantage that it can provide a momentum to the electrolyte ions to reach the interior of the electrodes because of its hollow structure. This leads to a high coefficient of utilization of the electrode material [16].A longer polymer conjugated backbone also offers better conducting pathways, which manifests in improved capacitance [17].A hybrid graphene aerogel with PAni nanotubes (PAniNTs) acting as spacer presents an ideal positive electrode material for ASCs to boost the energy.

Till date, development of materials with high specific surface area has remained the focus of research where supercapacitor electrodes are concerned. Supercapacitors store energy primarily at the electrode/electrolyte interface. Electrode materials should therefore be sufficiently conductive so as to transport charge carriers to the electrolyte interface.When graphene sheets agglomerate, it is associated with a decrease in electrical conductivity and an increase in internal resistance related to the contact resistance between the electrodes and the current collectors, and is responsible for an Ohmic (*IR*) drop. Hence, it is imperative that the *IR* drop should be minimized in order to enhance the electrical conductivity of the electrodes and also to decrease the contact resistance. The decrease in electrical conductivity is also caused by continuous charging and discharging due to formation of defect sites [18]. Functionalizing graphene with conductive materials is, hence, necessary to augment its conductivity. It is a celebrated fact that metals like silver (Ag) are one of the most conductive materials owing to high free-electron density. To increase the electrical conductivity and reduce the internal resistance, embedding Ag into the graphene aerogel is highly advantageous and can be applied as an anodic material. The limited literature available on metal nanoparticles doped graphene as negative electrode features palladium nanoparticle decorated graphene aerogel [18], three-dimensional Ag-graphene hybrid hydrogel [19] and graphene/Ag hybrid thin film [20].In this study, we make an attempt to prepare Ag nanorods (AgNRs) and incorporate them into the

graphene aerogel network to take advantage of both the high conductivity of Ag and high surface area of the aerogel.

Nanocomposites of graphene as flexible electrodes are well-accepted [21,22].In this work, we have functionalized reduced graphene oxide aerogel (rGOA) to obtain two different types of nanocomposites: AgNR/rGO aerogel as negative electrode and PAniNT/rGO aerogel as positive electrode for flexible all-solid-state ASC. A wide potential window of 1.8 V is achieved with the assembled device with extraordinary mechanical flexibility.

4.2 Materials and methods

4.2.1 Chemicals

Graphite flakes, sodium nitrate ($NaNO_3$), potassium permanganate ($KMnO_4$), ferric chloride ($FeCl_3$) ethylene glycol, silver nitrate ($AgNO_3$), polyvinylpyrrolidone (PVP), resorcinol, formaldehyde (HCHO), sodium carbonate (Na_2CO_3), poly(vinyl alcohol) (PVA), sulfuric acid (H_2SO_4), hydrogen peroxide (H_2O_2), hydrochloric acid (HCl), acetone, ethanol and Nafion were purchased from Merck.

4.2.2 Synthesis of graphene oxide (GO)

GO was prepared as a starting material for aerogel synthesis by modified Hummers' method [23].In a typical synthesis procedure, 23 mL concentrated H_2SO_4 was added to 1 g graphite flakes and 0.5 g $NaNO_3$, and stirred for 4 h in an ice bath. Following that, 3 g $KMnO_4$ was added to the reaction slowly and then diluted with 184 mL distilled water. The ice bath was removed at the end of 2 h and the reaction was stirred at 35 ℃ for another 2 h. Subsequently, it was refluxed at 98 ℃ for 10-15 min, followed by lowering the temperature to 25-30 ℃, whereupon the solution turned brown. After stirring for 2 h at that temperature, 8 mL H_2O_2 was added with the resulting solution turning bright yellow. The product GO, was washed with 10% HCl solution and water, and dried.

4.2.3 Synthesis of PAniNT

PAniNTs were prepared by chemical oxidation polymerization of aniline described in *Section 2.2.2.1 of Chapter 2*.

4.2.4 Synthesis of AgNR

In a typical synthesis procedure adopted from Jiu *et al*.[24], 0.5 mL of 6×10^{-4} M $FeCl_3$ solution was prepared in ethylene glycol. Then, it was mixed with further 6 mL of

ethylene glycol, 0.052 M $AgNO_3$ and 0.067 M PVP. PVP acted both as the reducing agent and the solvent. The reaction was then heated at 150 ℃ for 1.5 h. The resulting solution was repeatedly diluted with large volume of acetone and ethanol, followed by centrifugation to remove the remaining PVP and other organic compounds formed in the reaction.

4.2.5 Synthesis of AgNR functionalized and PAniNT functionalized rGOA

The AgNR/rGO aerogels were prepared by the procedure adopted from Cheng *et al*. with some modifications [25]. 20 mL GO suspension in distilled water with concentration of 10 mg mL^{-1} was prepared by sonicating it for 10 min. 0.337 g resorcinol, 0.362 g HCHO and 1.6 mg Na_2CO_3 were added to the suspension and stirred for 30 min. In a separate beaker, 20 mL suspension of 10 mg mL^{-1} AgNRs was prepared in distilled water by sonicating it for 30 min. Both the solutions were mixed and stirred for 10 min more, and then sealed and transferred to an oven maintained at 85 ℃ for 3 days. Subsequently, the AgNR/rGO hydrogel with feed weight ratio of AgNR to GO as 1:1, was obtained which was then washed with water, and freeze-dried for 24 h to completely remove the water and obtain AgNR/rGO aerogel. The synthesis procedure for obtaining PAniNT/rGO aerogel is similar to the one described above. 20 mL suspension of 10 mg mL^{-1} PAniNT was prepared and added to 20 mL GO suspension (10 mg mL^{-1}). The rest of the process was repeated to obtain PAniNT/rGO aerogel. For comparison, pristine rGOA was also synthesized by a similar procedure sans the addition of AgNRs or PAniNTs.

4.2.6 Fabrication of flexible ASC devices

Flexible polyethylene terephthalate substrates were washed ultrasonically with a solution of H_2O: NH_4OH: H_2O_2 = 5:1:1 volume ratio for 10 min, and thoroughly rinsed with water. A layer of silver metal was deposited on the substrate by thermal evaporation technique to act as current collector. The negative electrodes and positive electrodes were correspondingly fabricated by using AgNR/rGO aerogel and PAniNT/rGO aerogel dispersions in 0.5% Nafionsolution by doctor blade technique, wherein Nafion acted as a binder. To prepare polymer gel electrolyte (PGE), 1 g H_2SO_4 and 1g PVA were added in 10 mL distilled water and stirred at 85 ℃ till the solution became clear (approximately 2 h). The PGE was allowed to cool to room temperature. It was then slowly poured on the as-prepared electrodes and left undisturbed for 30 min. Afterwards, the electrodes were assembled into a flexible ASC and left for 24 h in a fume hood to vapourize the excess

water. H_2SO_4/PVA acted both as the PGE as well the separator in these devices. The entire fabrication process is represented schematically in **Scheme 4.1**.

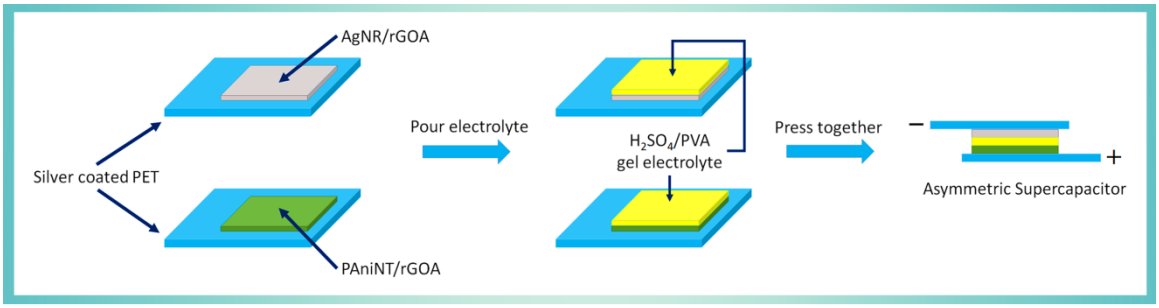

Scheme 4.1 Schematic representation of the device fabrication process.

4.2.7 Characterization and tests

Raman spectroscopy, scanning electron microscope (SEM), transmission electron microscope (TEM), cyclic voltammetry (CV) and electrochemical impedance spectroscopy (EIS) are used to characterize the materials. The value of C_{sp} was calculated from the CV data according to **relation (4.1)**:

$$C_{sp} = \frac{\int I' dV'}{\nu m' \Delta V'} \qquad \textbf{(4.1)}$$

where *I'*, *V'*, *v* and *m'* represents voltammetric current, potential in one sweep segment, scan rate and mass of active element in the electrodes respectively. Additionally, X-ray photoelectron spectra of the samples were recorded in a Kratos Axis-Ultra spectrometer. Nitrogen adsorption/desorption isotherms were obtained by a Quantachrome NOVA 1000E Brunauer-Emmett-Teller (BET) apparatus. The galvanostatic charge discharge (GCD) tests were carried out on the same instrument as CV (Bio-Logic SP-150 potentiostat). The C_{sp}values of the devices were calculated from the galvanostatic discharge curves by applying **relation (4.2)**:

$$C_{sp} = \frac{I'' \Delta t}{m' \Delta V''} \qquad \textbf{(4.2)}$$

where *I''*, *Δt*, *m'* and *ΔV''* represents discharge current, full discharge time, total mass of the active material in both the electrodes and potential change after complete discharge respectively. The values of *E* and power density (*P*) were calculated from **relations (4.3)** and **(4.4)**:

$$E = \frac{C_{sp} \Delta V''^2}{2} \qquad \textbf{(4.3)}$$

$$P = \frac{E}{\Delta t} \qquad \textbf{(4.4)}$$

4.3 Results and discussion

Graphene and its analogues are unique materials that can be used as a versatile building block for preparing three-dimensional graphene based architectures via self-assembly [26]. GO is an amphiphilic conjugated material having a hydrophobic basal plane and hydrophilic oxygenated groups. The oxygenated groups present in GO include phenol epoxy and epoxide groups on the basal plane and ionizable carboxylic acid groups around the edges. The hydrophilicity rendered by acid groups on the ionized edge helps in dispersion of GO in the aqueous medium through weak dipole and quadrupole van der Waals interaction. The oxygenated groups can also interact with the AgNRs via physisorption or electrostatic binding [27].The aromatic regions, on the other hand, can be utilized to attach PAniNTs through π-π stacking interactions.

The functionalized graphene based aerogels used in our study as the electrode materials were prepared by self-assembly driven sol-gel technique. Gelation of the reaction mixture was promoted by Na_2CO_3 catalyst, whereas cross-linking of the individual rGO sheets was facilitated by the hydrophobic-hydrophilic interaction between the van der Waals' forces (inter planar) and electrostatic repulsion [28].

4.3.1 Raman spectra analyses. In case of graphitic materials like GO and rGOA, two prominent bands are observed in their Raman spectra **Figure 4.1**. The first band is the D band at 1381 cm^{-1} which is ascribed to typical defects arising from structural edge effects, due to a breathing mode of k-point phonons with A_{1g} symmetry. The second band at 1611 cm^{-1} is called the G band which is ascribed to the graphitic structure and corresponds to the first order scattering of E_{2g} phonon of sp^2 carbon atoms at the Brillouin zone center [29]. The reduction of GO to rGO during the aerogel formation is indicated by the value of ratio of intensities of D and G bands, denoted by I_D/I_G. In this case, this value changes from 0.98 in GO to 1.15 in rGOA. The increase in the I_D/I_Gratio suggests that during reduction, the functional groups containing oxygen are partially reduced. The value of I_D/I_Gratio further increases to 1.28 in AgNR/rGO aerogel. The difference in the Raman peak intensities between rGOA and AgNR/rGO aerogel is an indication that the transfer of electrons from AgNRs to GO nanosheets is influenced by the interfacing structures between them. When Ag nanoparticles form a direct contact with graphene derivatives, electron transfer takes place from Ag to sp^2 carbon domains of graphene derivatives, because of the smaller work function of Ag nanoparticles (4.2 eV) as compared to that of graphene derivatives (> 4.8 eV, depending on their chemical structures). This process changes the work function of Ag nanoparticles in the composite, which is reflected in the Raman spectra [30].Additionally, the D band and the G band shift in the opposite directions, which can be

attributed to the *n*-type doping introduced by AgNRs when they are intercalated into rGOA matrix [31].When PAniNT/rGO aerogel is formed, its Raman spectrum shows additional peaks due to presence of PAniNT. The peaks at 1350, 1550 and 1620 cm^{-1} are indicative of semi-benzoid polaronic ν(C-N+•), imine ν(C=N) vibration and ν(C-C) vibration band respectively. Another peak at 1200 cm^{-1} appears due to C-H in plane bending vibration of quinoid ring [32].

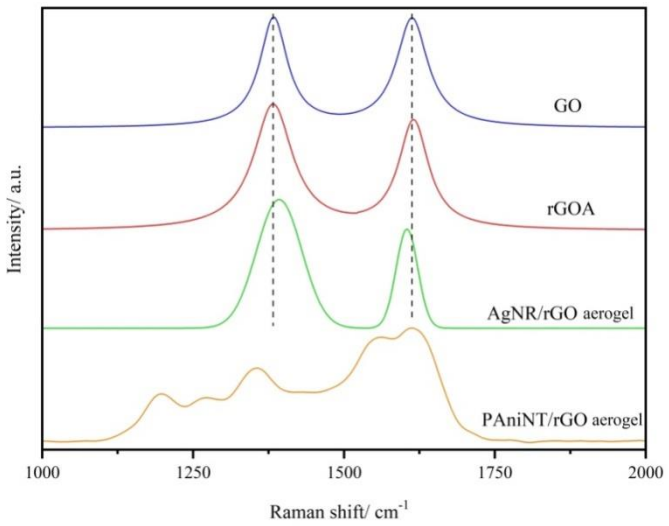

Figure 4.1 Raman spectra of GO, rGOA, AgNR/rGO aerogel and PAniNT/rGO aerogel.

4.3.2 X-ray photoelectron spectroscopy (XPS) analyses.Figure 4.2 displays the high resolution XPS patterns of GO, rGOA, AgNR/rGO aerogel and PAniNT/rGO aerogel. XPS is employed as a characterization tool to assess the extent of the reduction of GO to rGO during the aerogel formation process by analyzing the core-level C *1s* peaks. XPS patterns of all the materials can be deconvulated into four characteristic peaks according to their binding energies, corresponding to C–C/ C=C in the aromatic rings (284.7 eV), C–O of epoxy and alkoxy groups (286.4 eV), C=O groups (288.2 eV) and O–C=O groups (290.0 eV) **(Figure 4.2 (a-c, e)** [33]. A noteworthy decrease in the intensities of peaks of carbon binding to oxygen is clearly visible. Such an observation can be attributed to the partial removal of oxygenated moieties. Meanwhile, the intensity of the C–C/ C=C peak increases indicating that the sp^2structure has been reinstated. The surface composition of the AgNR/rGO aerogel also shows the *3d* spectral region of Ag. The deconvulated spectrum shows a doublet at 368.8 eV ($3d_{5/2}$) and 374.9 eV ($3d_{3/2}$), caused primarily by spin−orbit coupling **(Figure 4.2 (d))** [27]. In the C *1s* spectrum of PAniNT/rGO aerogel, the presence of PAniNT is revealed by the appearance of an additional peak at 286 eV (C–N) **(Figure 4.2 (e))**. Studies on the core-level N *1s* region of PAniNT/rGO aerogel indicate the existence of three different peaks: quinoid amine (=N– at 398.8 eV), benzenoid amine (N–H

at 399.5 eV), and nitrogen cationic radical ($N^{+\bullet}$at 401.2 eV) **(Figure 4.2 (f))** [34]. The presence of $N^{+\bullet}$suggests that it can improve the conductivity of the composites.

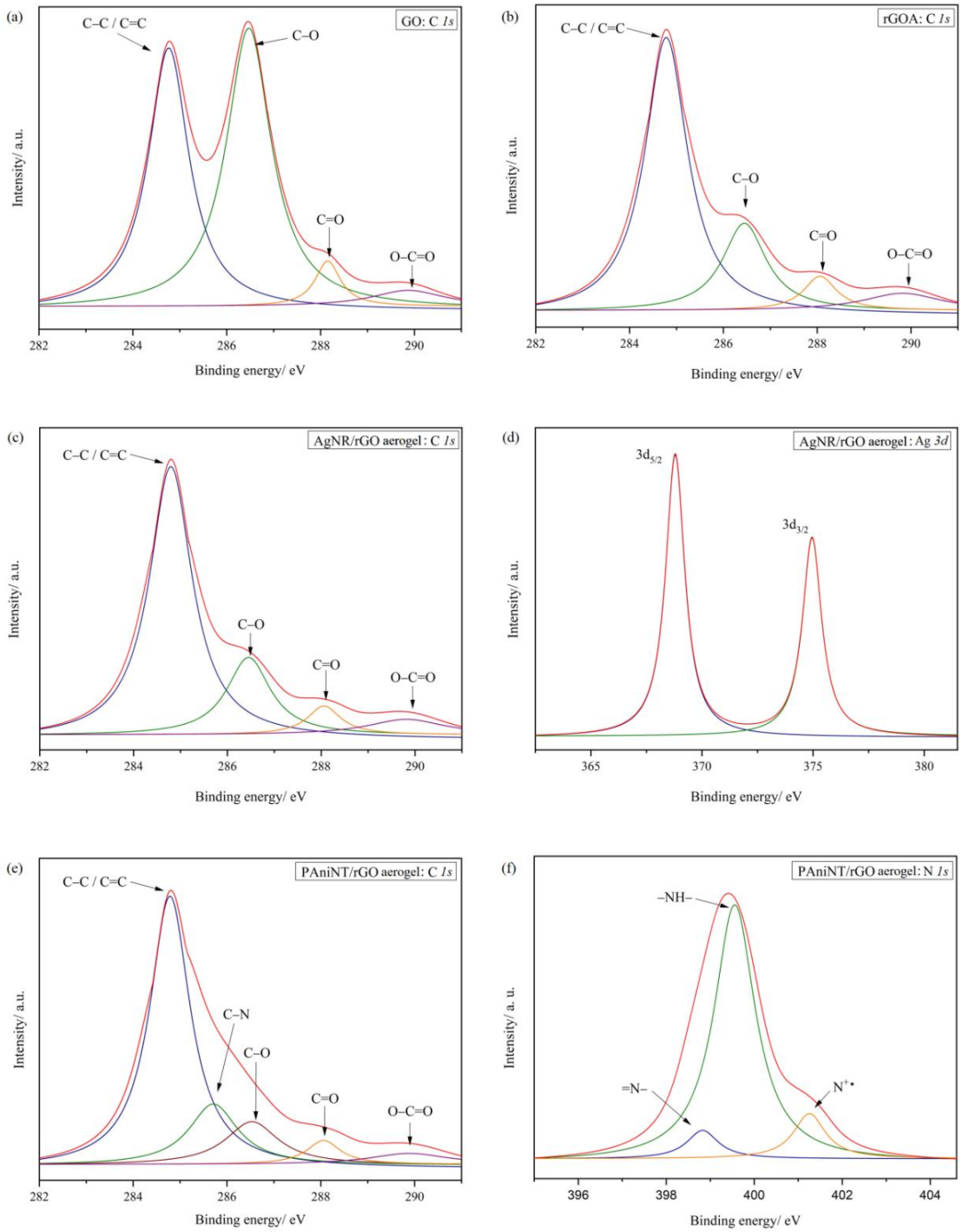

Figure 4.2 Core-level XPS patterns of **(a)** C *1s* of GO, **(b)** C *1s* ofrGOA, **(c)** C *1s* of AgNR/rGO aerogel, ***(d)***Ag *3d* of AgNR/rGO aerogel, **(e)** C *1s* of PAniNT/rGO aerogel and **(f)** N *1s* of PAniNT/ rGO aerogel.

4.3.3 BET surface area and pore size analyses.Figure 4.3 (a) shows the BET isotherms of rGO aerogel and AgNR/rGO aerogels with three different feed weight ratios of AgNR to GO: AgNR/rGOA13 (1:3), AgNR/rGOA11 (1:1) and AgNR/rGOA31 (3:1). PAniNT/rGO aerogels with similar feed weight ratios of PAniNT to GO: PAniNT/rGOA13 (1:3), PAniNT/rGOA11 (1:1) and PAniNT/rGOA31 (3:1) are shown in **Figure 4.3 (b)**. The nitrogen adsorption-desorption curves are used to calculate the specific surface area of the samples. The profiles of the hysteresis loops in all the cases are typical of Type-IV isotherm characteristic of mesoporous materials. The specific surface area of pure rGOA is 171 m^2 g^{-1}. Interestingly, in case of AgNR/rGO aerogels and PAniNT/rGO aerogels, increased specific surface areas can be seen. The BET surface area of AgNR/rGOA11 is 203 m^2 g^{-1}, which is the highest amongst all the compositions containing AgNRs. On the other hand, the maximum specific surface area among all three PAniNT/rGO aerogels is shown by PAniNT/rGOA11 (298 m^2 g^{-1}). The overall increase in the surface area of the composite aerogels in comparison to rGOA indicates that the presence of spacers can prevent the restacking problem of rGO sheets to a significant extent. Barrett-Joyner-Halenda (BJH) method is employed to calculate the pore size distribution of the aerogels. The insets of **Figure 4.3** shows that majority of the pore volume as determined from the desorption curves lies in the 2-70 nm range. The maximum intensity peak of rGOA and the AgNR functionalized rGO aerogels is centered at around 3.7 nm, while a shift to approximately 10.0 nm is observed for PAniNT functionalized rGO aerogels.

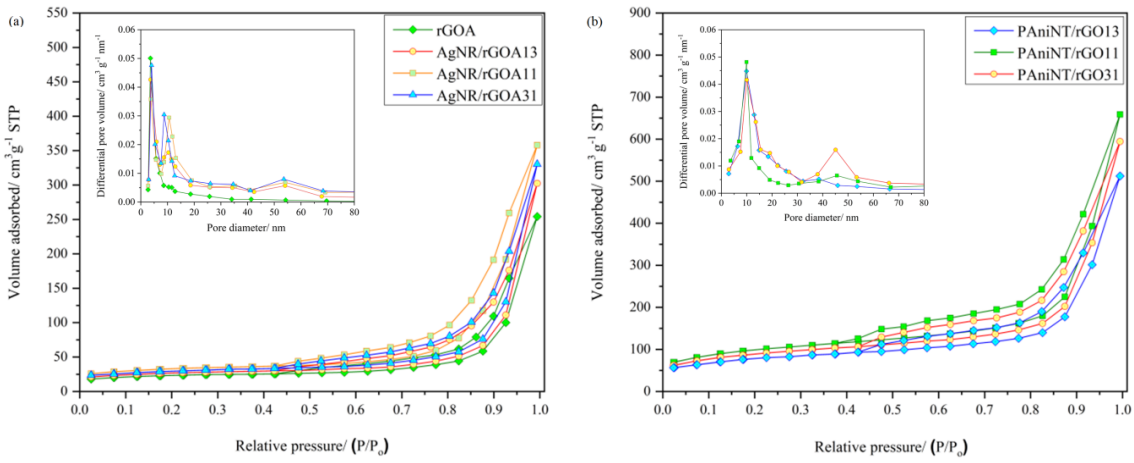

Figure 4.3 BET isotherms of **(a)** rGOA and AgNR/rGO aerogels with different compositions, and **(b)** PAniNT/rGO aerogels with varying compositions (inset: the corresponding pore size distributions).

4.3.4 Morphological study of the aerogels. SEM micrograph of GO shows typical thick layers of graphene along with outer layers that have delaminated (**Figure 4.4 (a)**). GO normally resembles the two-dimensional graphene structure, with oxygenated groups on its basal plane. rGOA shows three-dimensional porous structure of small graphene layers in its SEM image (**Figure 4.4 (b)**). Such architecture is highly advantageous for energy storage systems because they enable rapid electrolyte transport. The resorcinol-formaldehyde (R-F) solution initiated polymerization technique for aerogel preparation was originally developed for carbon aerogel [35] and is the reason why Cheng *et al.* observed carbon particles in their aerogels that prevented the aggregation of graphene. However, such particles are not seen in our work. It can be rationalized that when the amount of R-F mixture is sufficiently low in comparison to

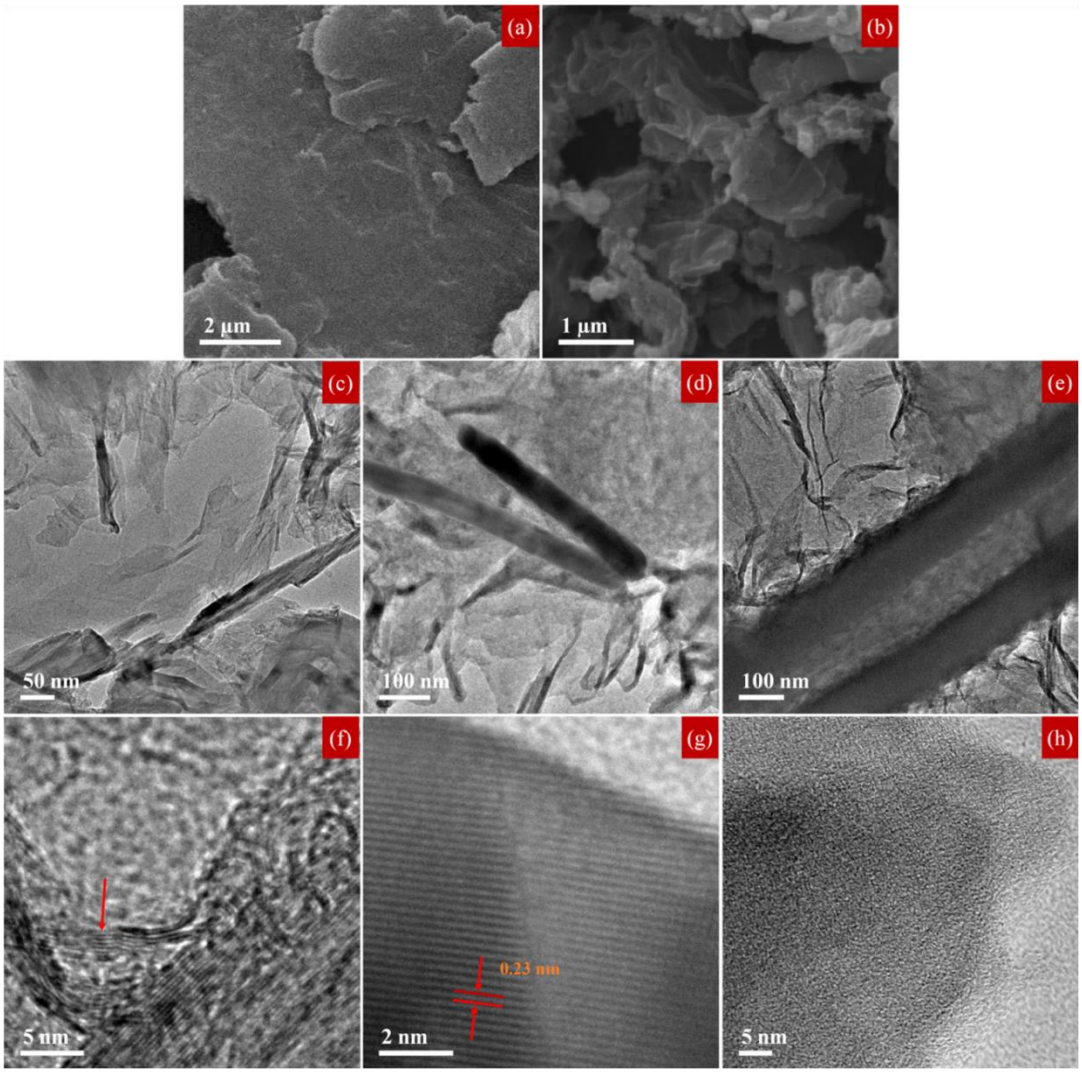

Figure 4.4 SEM micrographs of **(a)** GO and **(b)** rGOA, TEM micrographs of **(c)** rGOA, **(d)** AgNR/rGO aerogel and **(e)** PAniNT/rGO aerogel, and HRTEM images of **(f)** rGOA, **(g)** AgNR/rGO aerogel and **(h)** PAniNT/rGO aerogel.

rGO, polymerization takes place at the oxygenated ends of rGO. As a result, individual carbon particles no longer exist but rather aid in cross-linking the rGOA network [36]. A similar structure with wrinkled surfaces and sharp edges is also seen in the TEM image of rGOA (**Figure 4.4 (c)**). The high resolution TEM (HRTEM) image of rGOA reveals that the wrinkled surfaces are comprised of multi layers of graphene **(Figure 4.4 (f))**. A TEM image of the AgNR/rGO aerogel **(Figure 4.4 (d))** shows randomly oriented AgNRs distributed between graphene layers, thereby inhibiting its aggregation. The image clearly shows nanorod morphology of the Ag nanoparticles with an average diameter of 50 nm. A HRTEM micrograph demonstrates the lattice fringes of AgNRs with an inter-planar distance calculated to be about 0.23 nm **(Figure 4.4 (g))**. The value of d-spacing corresponds to the (111) crystallographic planes of Ag. In the TEM image of PAniNT/rGO aerogel, PAniNT can be seen attached to the rGO sheets without any aggregation (**Figure 4.4 (e)**). π-π stacking between the rGO sheets and PAniNT is the prominent interaction by which PAniNTs attach to rGO. Consequently, it prevents the restacking of rGO sheets. The HRTEM image of PAniNT/rGO aerogel is conspicuous by the absence of any crystallinity in the PAniNT structure **(Figure 4.4 (h))**.

4.3.5 AgNR/rGO aerogel as negative electrode material. Considering the intent to obtain a highly conductive material, the DC electrical conductivities of the AgNR doped rGO aerogels with different compositions were measured by using the four probe technique. Pristine rGOA shows bulk conductivity of 1.3 S m^{-1}. Doping of rGOA with AgNRs can lead to a dramatic increase in its conductivity. The structure of rGO can be divided into two regions: one is oxygen-rich and the other is oxygen-poor (graphitic). The oxygen-rich region is highly resistive and this interfacial region between two graphitic domains can trap the charge carriers. However, the introduction of one-dimensional nanostructures like AgNRs can connect the graphitic domains by bridging the oxygen-rich regions. Thus the detrimental effect of the resistive oxygen-rich regions can be overcome by electrically connecting the graphitic domains via AgNRs [37]. As the amount of AgNRs is increased in the composite, their conductivities also increase. AgNR/rGOA11 shows the maximum conductivity with a value of 14.7 S m^{-1}. As the amount of the rGOA is superseded by that of AgNRs, the formation of a homogeneous AgNR network is prevented by the lack of rGOA surface for their loading. Hence, the electrical properties do not improve after a threshold is reached.

CV was employed as a diagnostic tool to measure the electrochemical performance of the AgNR/rGO aerogels as an electrode material by using a three electrode system with AgNR/rGO aerogel serving as the working electrode **(Figure 4.5**

(a)). A Pt wire and an Ag/AgCl (saturated KCl) system dipped into 1 M H_2SO_4 solution served as the counter electrode, reference electrode and electrolyte respectively.

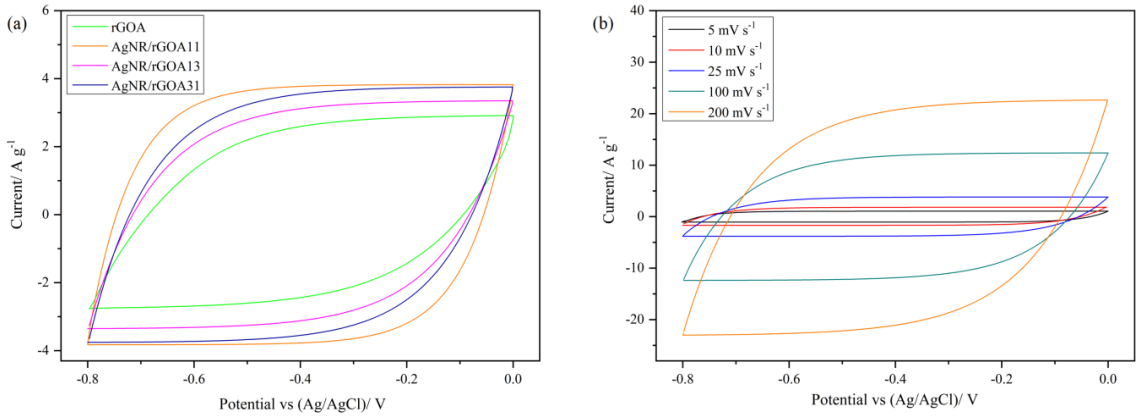

Figure 4.5 (a) CV curves of pristine rGOA and different AgNR/rGO aerogel electrodes at a scan rate of 25 mV s^{-1} and **(b)** CV curves of AgNR/rGOA electrode at different scan rates.

The pristine rGOA exhibits a quasi-rectangular curve, which is the signature of an EDLC. Such type of capacitance arises due charge redistribution at the electrochemical double layer of the system.Generally, the electrolyte is electrically neutral when it is away from any solid surfaces, satisfying the **relation 4.5** [38].

$$\sum_i z_i c_i = 0 \qquad \textbf{(4.5)}$$

wherez_i represents the charge on species i and c_i is the concentration of species i. But when an external potential is such that no current flows in the cell (non-faradaic process), the potential must remain uniform in the electrolytic solution. This leaves the electrode/electrolyte interface as the only place where the potential can change inside the cell. To accommodate this change in potential, redistribution of charges take place at the double layer. Within the potential window of -0.8 V to 0 V, the charging process at the negative electrode can be expressed in terms of **relation 4.6** [3].

$$rGO + e^- + H^+ \leftrightarrow rGO/H \qquad \textbf{(4.6)}$$

Under these conditions, no charge-transfer reactions occur at the electrode/electrolyte interface because of thermodynamic or kinetic restrictions. Nonetheless, processes such as adsorption and desorption can occur easily leading to charge redistribution. With the incorporation of AgNRs in the rGOA matrix, the shape of the curve becomes progressively rectangular. Simultaneously, an increase in the current density and

integrated area is observed, that directly manifests in an increase in its capacitive behavior. The best capacitive behavior amongst the three composite aerogels (i.e., AgNR/rGOA13, AgNR/rGOA11 and AgNR/rGOA31) is shown by AgNR/rGOA11 (C_{sp} = 296.8 F g^{-1} at 25 mV s^{-1}). This result is in perfect agreement with the conductivity measurements which establishes AgNR/rGOA11 as the composite with the highest conductivity. For the sake of convenience, the aerogel with feed weight ratio of 1:1 will be denoted by AgNR/rGOA only for the remaining part of this paper. The enhanced electrochemical behavior of the composite material can be attributed to the conductive AgNRs which facilitate fast charge propagation as well as prevent re-stacking of the individual graphene sheets [20]. In general, restacking of graphene sheets leaves the inter-graphene pore sizes too small to be properly accessed by the electrolyte ions [39].However, the three-dimensional porous aerogel network prevents the deterioration of graphene structure to a large extent and also provides multi-dimensional charge transport pathways and better access to the electrolyte [40].The composite aerogel retains its quasi-rectangular shape when the scan rate is increased from 5 to 200 mV s^{-1}**(Figure 4.5 (b)),** reiterating the excellent charge transport process.

4.3.6 PAniNT/rGO aerogel as positive electrode material.Figure 4.6 (a) shows the CV curves of pristine PAniNT and various PAniNT/rGO aerogels as working electrodes within the potential range of -0.2 V to 0.8 V. The CV curve of pure PAniNT, obtained by a three electrode configuration, displays peaks for redox pairs related to their pseudo-capacitive nature that store charge by faradaic process. In such a situation, oxidation or reduction reaction occurs at the electrode with concomitant faradaic charge transfer taking place across the electrode/electrolyte interface. The deviation from rectangular shape in a pseudo-capacitor can be explained on the basis of the following relations [41].The correlation between potential (*E''*) and the extent of fractional coverage of the electrode surface or inner structure (*X*) is a Nernst-like equation **(relation (4.7))**.

$$E'' \sim E_o - \frac{RT}{nF}\ln\left(\frac{X}{1-X}\right) \quad \textbf{(4.7)}$$

$$C = \left(\frac{n\prime F}{M}\right)\frac{X}{E''} \quad \textbf{(4.8)}$$

where*n'* and *M* are the number of electrons and molecular weight of the active material respectively. Capacitance can be defined in regions where the plot of **relation (4.8)** is linear. However, this plot is not linear for a redox capacitor, and hence the CV curve no longer remains rectangular. The charge storage in PAniNT occurs by alternating the

polymer between two doping states. At the positive electrode, during the charging process (oxidative *p*-doping), PAniNT becomes polycationic and negative ions (A^-) from the electrolyte are intercalated into the polymer backbone to maintain electro-neutrality **(relation (4.9))**.

$$(PAniNT)_a + xA^- \leftrightarrow [(PAniNT)_{x+a}(A^-)_x] + xe^- \quad \textbf{(4.9)}$$

where*a* is the degree of polymerization. The entire PAniNT chain is involved in the doping/ de-doping process. Although it is beneficial for obtaining high capacitance, but it may also cause damage to the polymer structure, shortening its life cycle. Thus, coupling PAni with rGO helps in improving the life cycle of the electrode [42].

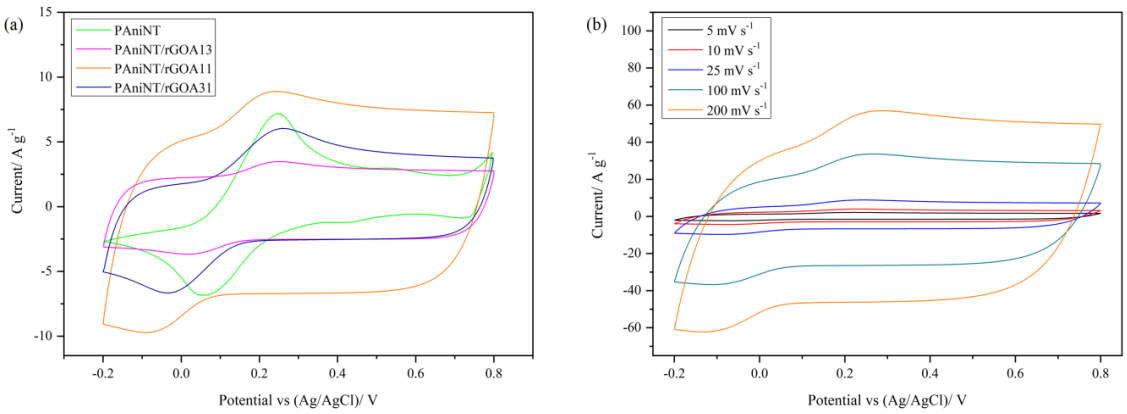

Figure 4.6 (a) CV curves of pristine PAniNT and various PAniNT/rGO aerogel electrodes at a scan rate of 25 mV $s^{-1}$and **(b)** CV curves of PAninT/rGOA electrode at different scan rates.

The CV plot of the composite PAniNT/rGO aerogels show quasi-rectangular shape with faradaic humps. The peaks are broad and have a small peak-to-peak voltage separation. Two types of direct interactions are prominent in PAniNT/rGOA: electrostatic interaction between the positive charges present along the PAniNT chains and the negative charges of the carboxylic groups present on the surface of rGO, and π-π interaction. The negative charges on rGO facilitate the removal of electrons from PAniNT via oxidation, causing a negative shift of the peak potentials in comparison to pristine PAniNT. Secondly, π-π stacking interactions cause delocalization of electrons along the PAniNT chain. As a consequence, the number of monomers involved in each electron transfer decreases. Since fewer number of monomer units are involved, PAniNT shows greater capacity for electron transfer. Thus, there is an apparent increase in the

capacitance of PAniNT/rGO aerogels with the incorporation of PAniNT. The aerogel structure with high accessible surface area provides a large number of electrochemical action sites and also contributes to fast electrolyte ion transfer [17].The maximum value of $C_{sp}$is demonstrated by PAniNT/rGOA11 composition with a value of 377.1 F g^{-1} obtained at 25 mV s^{-1}. Since this composition exhibits the best behavior in terms of capacitance as well as surface area, the same composition will be used for further evaluation and will be denoted simply by PAniNT/rGOA for the rest of the paper. Over a wide scan rate range from 5 to 200 mV s^{-1}, the shape of the curves for PAniNT/rGOA remain quasi-rectangular containing the faradaic peaks suggesting good capacitive behavior **(Figure 4.6 (b)**).

4.3.7 Asymmetric supercapacitor. From the materials' perspective, two of the most important criteria for good capacitor performance are high specific surface area and good electronic or ionic conductivity. A large accessible surface area is essential since most of the charges are stored at the electrode surface or near it whilst higher conduction of charges through the electrode ensures high rate capability and low electrochemical series resistance (ESR) [3].These properties make graphene based materials a favorite candidate for application in supercapacitors. In the previous sections, the potential of rGO based composites as supercapacitor electrodes has already been established: AgNR/rGOA enables fast charge transport and PAniNT/rGOA provides higher pseudo-capacitance. Proceeding from that, test devices were prepared with PAniNT/rGOA as positive electrode and AgNR/rGOA as negative electrode denoted as PAniNT/rGOA//AgNR/rGOA. Considering the total cell voltage as the sum of the potential for the negative electrode and the positive electrode, the working potential window of the PAniNT/rGOA//AgNR/rGOA ASC can be extended upto 1.8 V. The charge stored by each electrode (q) is given by **relation (4.10)**.

$$q = C_{sp} \times \Delta V \times m' \qquad \textbf{(4.10)}$$

For an ASC, charge is balanced by $q_+ = q_-$. Hence, mass balance can be obtained by following **relation (4.11)**.

$$R = \frac{m'_+}{m'_-} = \frac{C_{sp-} \times \Delta V_-}{C_{sp+} \times \Delta V_+} \qquad \textbf{(4.11)}$$

According to the analysis of the capacitance and potential values, an optimal R = 0.63 is obtained.

Figure 4.7 (a) shows the CV curves of the PAniNT/rGOA//AgNR/rGOA ASCs at different potential ranges. The assembled devices show quasi-rectangular shape upto 1.8

V indicating the feasibility of the device to perform as a supercapacitor. **Figure 4.7 (b)** shows the CV curves of the ASC at different scan rates ranging from 5 mV s^{-1} to 200 mV s^{-1}. The profiles remain relatively rectangular without any apparent distortions.

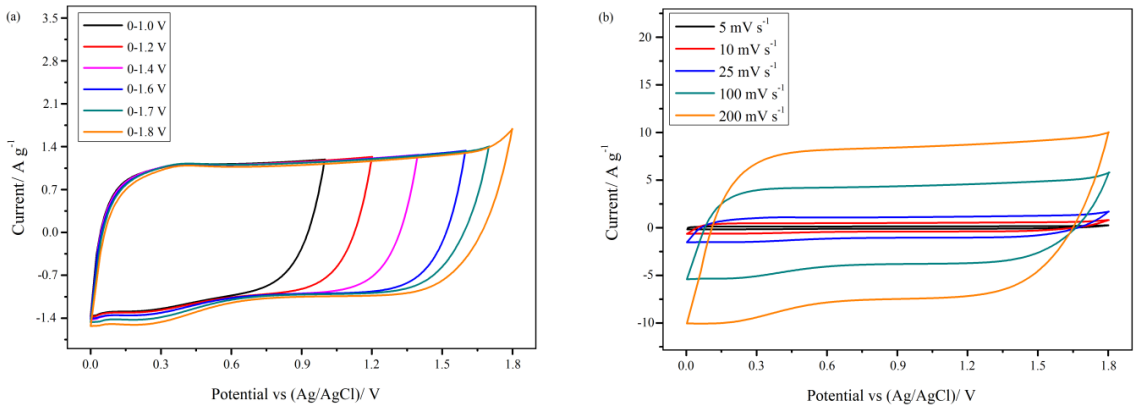

Figure 4.7(a) CV curves of PAniNT/rGOA//AgNR/rGOA ASC for different potential windows from 1 V to 1.8 V and **(b)** CV curves of the ASC at different scan rates.

The charge storage ability of ASC was further evaluated by GCD tests **(Figure 4.8 (a))**. A fast and reversible reaction is indicated by a moderately symmetrical triangular discharge curve. The capacitance obtained for this device is 117.4 F g^{-1} at 1 A g^{-1}.

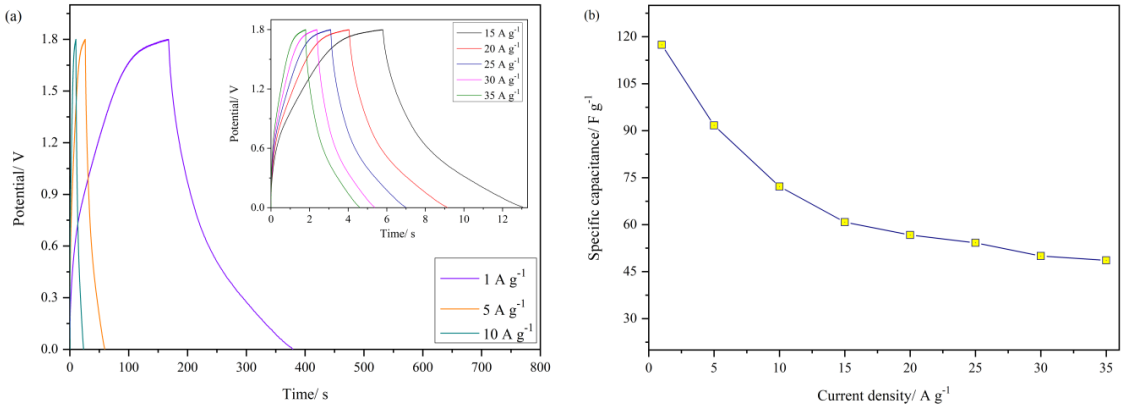

Figure 4.8(a) Charge-discharge tests of PAniNT/rGOA//AgNR/rGOA ASC at different current densities from 1 A g^{-1} to 10 A g^{-1} (inset: GCD curves at current densities from 15 A g^{-1} to 35 A g^{-1}), and**(b)** variation of C_{sp} with current densities.

On increasing the current densities gradually, the GCD curves remain consistently symmetrical implying excellent rate capability and reversibility of the device. With a ten-fold increase in current density from 1 A g^{-1} to 10 A g^{-1}, 61.5% of the capacitance is retained **(Figure 4.8 (b))**.

Ragone plot (energy density vs. power density) was used to evaluate the performance of our device with previous studies comprising of composites of graphene **(Figure 4.9)**. In our study, the ASC fabricated functionalized rGO aerogel shows a maximum energy density of 52.8 W h kg^{-1} at a power density of 0.9 kW kg^{-1}while maximum power density of 31.5 kW kg^{-1} is obtained for energy density of 21.9 Wh kg^{-1}. The obtained values compare favorably with previously reported values of asymmetric solid state devices [18,20,43,44].The exceptional capacitance behavior is a result of many factors including high specific surface area and mechanical robustness of the three-dimensional composite aerogel network. The inset shows the digital image of an LED bulb illuminated by connecting two ASCs in series.

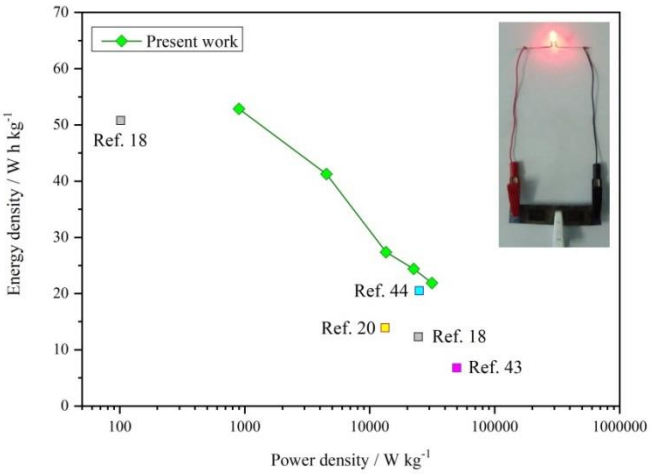

Figure 4.9 Ragone plot for performance comparison of the PAniNT/rGOA//AgNR/rGOA ASC with other graphene based ASCs; (inset: digital image of an illuminated LED bulb).

Figure 4.10 shows the Nyquist impedance plots of the AgNR/rGOA, PAniNT/rGOA and PAniNT/rGOA//AgNR/rGOA ASC fitted with an equivalent circuit comprising of resistive and capacitive elements. The impedance measurements for the individual electrodes were carried out using a three electrode configuration with liquid electrolyte while that of the ASC device was done using a two-electrode configuration with a PGE. The impedance for such systems can be calculated using **relation 4.12.**

$$Z = R_S + \frac{1}{j\omega C_{EDL} + \frac{1}{R_{CT}+W}} - \frac{j}{\omega C_F} \qquad \textbf{(4.12)}$$

whereR_S, R_{CT}, C_{EDL}, C_F and W represents equivalent series resistance, charge transfer resistance, electrochemical double layer capacitance, faradaic capacitance and Warburg impedance respectively.

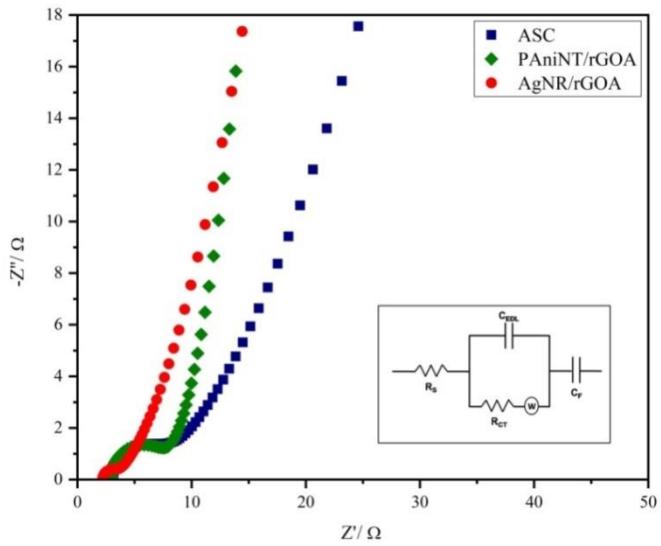

Figure 4.10 Nyquist plots of the ASC and individual electrodes fitted with an equivalent circuit as shown in the inset.

A typical Nyquist plot is divided into three regions**.** At high frequency region, the intercept on the *x* axis is a combined measure of resistance of the bulk resistance (R_b) of the electrolyte, intrinsic resistance (R_m) of the active material, and the contact resistance (R_c) at the interface of the active material, the electrolyte and the current collector, expressed in terms of R_S. The R_S value obtained for the ASC is 3.1 Ω. R_{CT} in parallel connection with C_{EDL} forms a semicircle in the real axis in the high-mid frequency region. Physically speaking, R_{CT} represents the total resistance to the electrolyte charges transferring on the electro-active electrode surface. Interfacial R_{CT} value of the device, obtained from the diameter of the semicircle is 4.9 Ω. The EIS curves of the positive and the negative electrode materials reveals that AgNR/rGOA shows R_S and R_{CT} values of 2.2 Ω and 1.2 Ω respectively while PAniNT/rGOA shows $R_S$and R_{CT} values of 2.9 Ω and 4.5 Ω respectively. In the low frequency region, there is a transition from semicircular shape to a long tail. In a perfect situation, a straight line parallel to the imaginary axis is representative of ideal capacitance while a deviation from this behavior is promoted by resistive elements of the non-ideal capacitance. A half semicircle and a slope almost parallel to *y* axis indicate low ion diffusion resistance in the electrode. The one-dimensional nanostructures play an important role in these devices as they offer direct current pathways [16].A direct inference from the EIS studies is that the solid-state devices show higher resistances and lower diffusion of electrolyte ions due to the gel nature of the electrolyte.

For practical application, it is crucial to evaluate the leakage current and self-discharge characteristics of the ASC devices. For testing the leakage current, the device was first charged to 1.8 V and then the leakage current was recorded by keeping it at the constant potential of 1.8 V for 24 h. A rapid drop in the leakage current is observed in the first few min after which it stabilizes at a constant value of 14 μA**(Figure 4.11 (a))**. For testing the self-discharge profile, the device was again charged to 1.8 V and held at that constant voltage for 30 min. Then the open-circuit voltage potential of the device was recorded using a digital multi-meter. The device retains approximately 58.3% of the initial potential after 24 h of self-discharge **(Figure 4.11 (b))**.

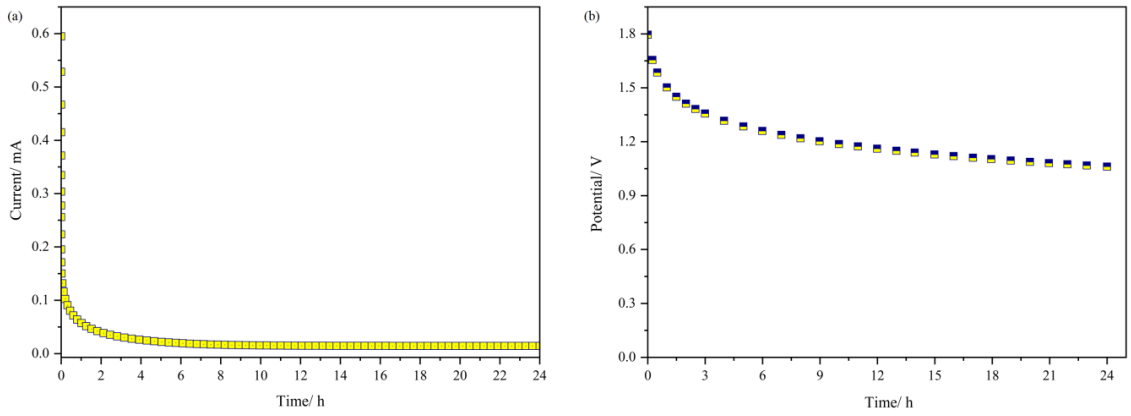

Figure 4.11(a) Leakage current curve and **(b)** self-discharge curve of the device.

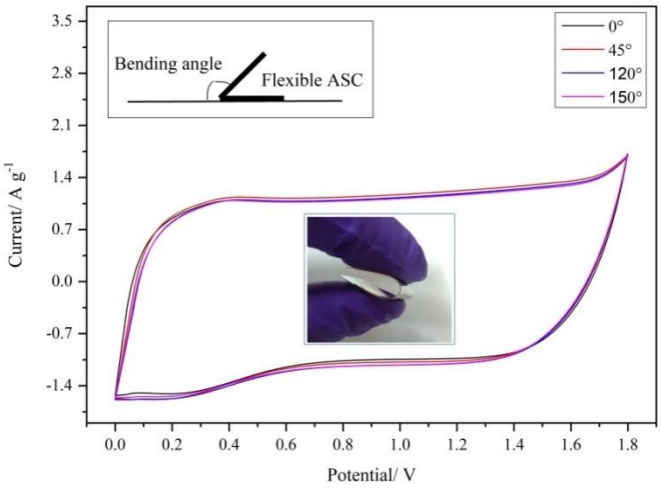

Figure 4.12 Cyclic voltammograms of ASCs with varying degrees of bending.

The potential application of the flexible ASC fabricated with functionalized rGO aerogels tested under different bending conditions shows no distinct difference in their electrochemical behavior **(Figure 4.12)**.

Furthermore, when the fabricated ASCs are tested for cycle stability, it is seen that the performance deteriorates by only 5.1% after 1000 cycles (**Figure 4.13 (a)**). When the ASC is subjected to repeated cycles of ingression and depletion of electrolyte ions, it causes stress resulting in alteration of the structure at microscopic level. Over a period of 2 months, only 6.8% decay is seen in its performance **(Figure 4.13 (b))**. Evaporation of water from the PGE might be the prominent reason for decay, as a consequence of which the ion movement is hampered.

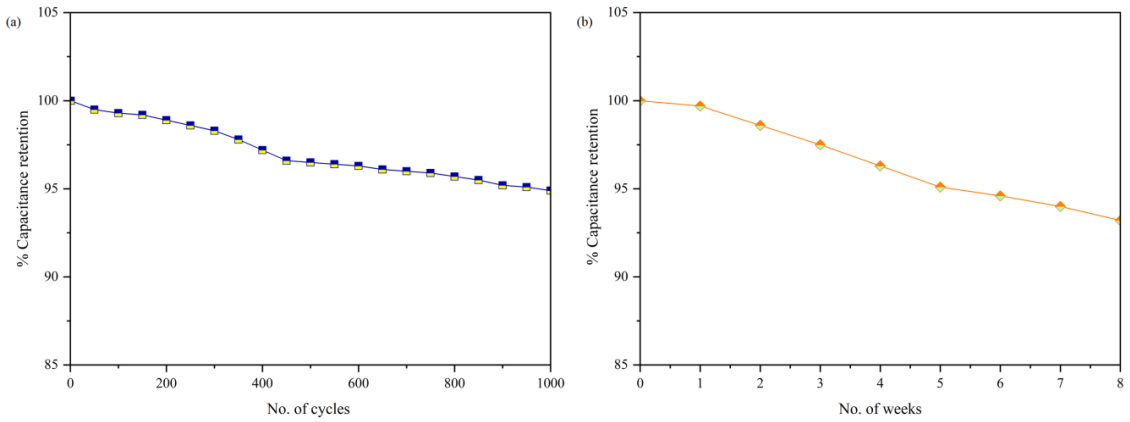

Figure 4.13 Performance of the ASC **(a)** during 1000 cycles and **(b)** over 2 months.

4.4 Conclusion

In this study, we have successfully functionalized rGO aerogel with AgNR and PAniNT to obtain two different types of composites: AgNR/rGOA and PAniNT/rGOA by a simple organic sol-gel technique. Each component has unique properties which make them highly suitable as active materials for supercapacitor electrodes. AgNRs improve the conductivity of the electrode while PAniNT offers a high pseudo-capacitance. A flexible device fabricated with AgNR/rGOA as negative electrode and PAniNT/rGOA as positive electrode with H_2SO_4/PVA PGE operates at a wide working potential window of 1.8 V. Composite formation leads to comprehensive exploitation of both double layer and faradaic capacitance of the constituting elements to obtain a synergistic effect. The flexibility studies also displayed negligible effect on the capacitor's performance even after bending it by 150º, indicating the composites' suitability as a candidate for flexible ASCs.

4.5 References

[1] Ge, J., Cheng, G., and Chen, L. Transparent and flexible electrodes and supercapacitors using polyaniline/single-walled carbon nanotube composite thin films. *Nanoscale*, 3(8):3084-3088, 2011.

[2] Choi, B. G., Hong, J., Hong, W. H., Hammond, P. T., and Park, H. Facilitated ion transport in all-solid-state flexible supercapacitors. *ACS Nano*, 5(9):7205-7213, 2011.

[3] Choudhary, N., Li, C., Moore, J., Nagaiah, N., Zhai, L., Jung, Y., and Thomas, J. Asymmetric supercapacitor electrodes and devices. *Advanced Materials*, 29(21):1605336, 2017.

[4] Xu, Y., Lin, Z., Huang, X., Liu, Y., Huang, Y., and Duan, X. Flexible solid-state supercapacitors based on three-dimensional graphene hydrogel films. *ACS Nano*, 7(5):4042-4049, 2013.

[5] Stoller, M. D., Park, S., Zhu, Y., An, J., and Ruoff, R. S. Graphene-based ultracapacitors. *Nano Letters*, 8(10):3498-3502, 2008.

[6] Shao, Q., Tang, J., Lin, Y., Li, J., Qin, F., Yuan, J., and Qin, L.-C. Carbon nanotube spaced graphene aerogels with enhanced capacitance in aqueous and ionic liquid electrolytes. *Journal of Power Sources*, 278:751-759, 2015.

[7] Conway, B. E. Electrochemical Behavior at Porous Electrodes; Applications to Capacitors. In *Electrochemical Supercapacitors*, pages 377-416, ISBN: 978-1-4757-3058-6. Springer US, Boston, MA, 2013.

[8] Kistler, S. S. Coherent expanded aerogels and jellies. *Nature*, 127(3211):741-741, 1931.

[9] Xu, Z., Zhang, Y., Li, P., and Gao, C. Strong, conductive, lightweight, neat graphene aerogel fibers with aligned pores. *ACS Nano*, 6(8):7103-7113, 2012.

[10] Ye, S., Feng, J., and Wu, P. Deposition of three-dimensional graphene aerogel on nickel foam as a binder-free supercapacitor electrode. *ACS Applied Materials and Interfaces*, 5(15):7122-7129, 2013.

[11] Zhang, Z., Chi, K., Xiao, F., and Wang, S. Advanced solid-state asymmetric supercapacitors based on 3D graphene/MnO_2 and graphene/polypyrrole hybrid architectures. *Journal of Materials Chemistry A*, 3(24):12828-12835, 2015.

[12] Gui, D., Liu, C., Chen, F., and Liu, J. Preparation of polyaniline/graphene oxide nanocomposite for the application of supercapacitor. *Applied Surface Science*, 307:172-177, 2014.

[13] Zhang, K., Zhang, L. L., Zhao, X. S., and Wu, J. Graphene/polyaniline nanofiber composites as supercapacitor electrodes. *Chemistry of Materials*, 22(4):1392-1401, 2010.

[14] Wang, K., Huang, J., and Wei, Z. Conducting polyaniline nanowire arrays for high

performance supercapacitors. *The Journal of Physical Chemistry C*, 114(17):8062-8067, 2010.

[15] Van Hoa, N., Quyen, T. T. H., Van Hieu, N., Ngoc, T. Q., Thinh, P. V., Dat, P. A., and Nguyen, H. T. T. Three-dimensional reduced graphene oxide-grafted polyaniline aerogel as an active material for high performance supercapacitors. *Synthetic Metals*, 223:192-198, 2017.

[16] Wang, Z. L., Guo, R., Li, G. R., Lu, H. L., Liu, Z. Q., Xiao, F. M., Zhang, M., and Tong, Y. X. Polyaniline nanotube arrays as high-performance flexible electrodes for electrochemical energy storage devices. *Journal of Materials Chemistry*, 22(6):2401-2404, 2012.

[17] Fan, X., Yang, Z., and Liu, Z. One-step synthesis of graphene/polyaniline nanotube composite for supercapacitor electrode. *Chinese Journal of Chemistry*, 34(1):107-113, 2016.

[18] Yu, Z., McInnis, M., Calderon, J., Seal, S., Zhai, L., and Thomas, J. Functionalized graphene aerogel composites for high-performance asymmetric supercapacitors. *Nano Energy*, 11:611-620, 2015.

[19] Quan, H., Shao, Y., Hou, C., Zhang, Q., Wang, H., and Li, Y. Room-temperature synthesis of 3-dimentional Ag-graphene hybrid hydrogel with promising electrochemical properties. *Materials Science and Engineering B: Solid-State Materials for Advanced Technology*, 178(11):769-774, 2013.

[20] Shao, Y., Wang, H., Zhang, Q., and Li, Y. High-performance flexible asymmetric supercapacitors based on 3D porous graphene/MnO_2 nanorod and graphene/Ag hybrid thin-film electrodes. *Journal of Materials Chemistry C*, 1(6):1245-1251, 2013.

[21] Ju, H. F., Song, W. L., and Fan, L. Z. Rational design of graphene/porous carbon aerogels for high-performance flexible all-solid-state supercapacitors. *Journal of Materials Chemistry A*, 2(28):10895-10903, 2014.

[22] Li, D., Feng, Y., Li, Y., Feng, W., and Hu, W. Hierarchical graphene oxide/polyaniline nanocomposites prepared by interfacial electrochemical polymerization for flexible solid-state supercapacitors. *Journal of Materials Chemistry A*, 3(5):2135-2143, 2014.

[23] Paulchamy, B., Arthi, G., and Lignesh, B. D. A simple approach to stepwise synthesis of graphene oxide nanomaterial. *Journal of Nanomedicine & Nanotechnology*, 06(01):1-4, 2015.

[24] Jiu, J., Murai, K., Kim, K., and Suganuma, K. Synthesis of silver nanorods and application for die attach material in devices. *Journal of Materials Science: Materials in Electronics*, 21(7):713-718, 2010.

[25] Cheng, W. Y., Wang, C. C., and Lu, S. Y. Graphene aerogels as a highly efficient counter

electrode material for dye-sensitized solar cells. *Carbon*, 54:291-299, 2013.

[26] Zhao, Z., Wang, X., Qiu, J., Lin, J., Xu, D., Zhang, C., Lv, M., and Yang, X. Three-dimensional graphene-based hydrogel/aerogel materials. *Reviews on Advanced Materials Science*, 36(2):137-151, 2014.

[27] Shao, W., Liu, X., Min, H., Dong, G., Feng, Q., and Zuo, S. Preparation, characterization, and antibacterial activity of silver nanoparticle-decorated graphene oxide nanocomposite. *ACS Applied Materials and Interfaces*, 7(12):6966-6973, 2015.

[28] Zeng, M., Wang, W. L., and Bai, X. D. Preparing three-dimensional graphene architectures: Review of recent developments. *Chinese Physics B*, 22(9):098105, 2013.

[29] Xu, C., Shi, X., Ji, A., Shi, L., Zhou, C., and Cui, Y. Fabrication and characteristics of reduced graphene oxide produced with different green reductants. *PLoS ONE*, 10(12):e0144842, 2015.

[30] Kim, Y. K., Ok, G., Choi, S. W., Jang, H., and Min, D. H. The interfacing structural effect of Ag/graphene oxide nanohybrid films on surface enhanced Raman scattering. *Nanoscale*, 9(18):5872-5878, 2017.

[31] Sun, S. and Wu, P. Competitive surface-enhanced Raman scattering effects in noble metal nanoparticle-decorated graphene sheets. *Physical Chemistry Chemical Physics*, 13(47):21116-21120, 2011.

[32] Wang, H., Hao, Q., Yang, X., Lu, L., and Wang, X. A nanostructured graphene/polyaniline hybrid material for supercapacitors. *Nanoscale*, 2(10):2164-2170, 2010.

[33] Feng, X. M., Li, R. M., Ma, Y. W., Chen, R. F., Shi, N. E., Fan, Q. L., and Huang, W. One-step electrochemical synthesis of graphene/polyaniline composite film and its applications. *Advanced Functional Materials*, 21(15):2989-2996, 2011.

[34] Yang, Y., Xi, Y., Li, J., Wei, G., Klyui, N. I., and Han, W. Flexible supercapacitors based on polyaniline arrays coated graphene aerogel electrodes. *Nanoscale Research Letters*, 12(1):394, 2017.

[35] Worsley, M. A., Pauzauskie, P. J., Olson, T. Y., Biener, J., Satcher, J. H., and Baumann, T. F. Synthesis of graphene aerogel with high electrical conductivity. *Journal of the American Chemical Society*, 132(40):14067-14069, 2010.

[36] Tamon, H., Ishizaka, H., Mikami, M., and Okazaki, M. Porous structure of organic and carbon aerogels synthesized by sol-gel polycondensation of resorcinol with formaldehyde. *Carbon*, 35(6):791-796, 1997.

[37] Wu, C., Fang, L., Huang, X., and Jiang, P. Three-dimensional highly conductive graphene-silver nanowire hybrid foams for flexible and stretchable conductors. *ACS Applied Materials and Interfaces*, 6(23):21026-21034, 2014.

[38] Orazem, M. E. and Tribollet, B. Electrochemistry. In *Electrochemical impedance spectroscopy*, pages 73-96, ISBN:9781118527399. John Wiley & Sons, 2011.

[39] Liu, C., Yu, Z., Neff, D., Zhamu, A., and Jang, B. Z. Graphene-based supercapacitor with an ultrahigh energy density. *Nano Letters*, 10(12):4863-4868, 2010.

[40] Ke, Q. and Wang, J. Graphene-based materials for supercapacitor electrodes – A review. *Journal of Materiomics*, 2(1):37-54, 2016.

[41] Augustyn, V., Simon, P., and Dunn, B. Pseudocapacitive oxide materials for high-rate electrochemical energy storage. *Energy and Environmental Science*, 7(5):1597-1614, 2014.

[42] Wang, H., Lin, J., and Shen, Z. X. Polyaniline (PANi) based electrode materials for energy storage and conversion. *Journal of Science: Advanced Materials and Devices*, 1(3):225-255, 2016.